

Capillary and Viscous Fracturing During Drainage in Porous Media

Francisco J. Carrillo*

Department of Chemical and Biological Engineering, Princeton University, Princeton, NJ, USA

Ian C. Bourg†

*Department of Civil and Environmental Engineering,
Princeton University, Princeton, NJ, USA*

and

High Meadows Environmental Institute, Princeton University, Princeton, NJ, USA

(Dated: April 16, 2022)

We study the transition from fluid invasion to capillary and viscous fracturing during drainage in porous media. To do so, we use our newly developed Multiphase Darcy-Brinkman-Biot framework to examine multiphase flow in deformable porous media in a broad range of flow, wettability, and solid rheology conditions. We demonstrate the existence of two fracturing transitions controlled by non-dimensional numbers that quantify the balance of viscous, capillary, and structural forces in the porous medium. We then use these parameters to establish a phase diagram for material failure caused by multiphase flow.

I. INTRODUCTION

Multiphase flow in deformable porous media is a ubiquitous phenomenon in natural and engineered systems. Notably, it underlies key processes in water and energy resource engineering including membrane filtration, soil wetting/drying, unconventional hydrocarbon recovery, and geologic carbon sequestration [1–3]. In these areas, a key obstacle to more accurate representations of the systems of interest is our limited fundamental understanding of the transition from fluid invasion to flow-induced fracturing.

The literature on *multiphase* flow within *static* porous media is extensive and includes detailed examinations of the influence of wettability, viscosity, and flow rate on flow in unsaturated media. In particular, existing studies have demonstrated how capillary forces give rise to differences between drainage and imbibition [4]; how the ratio of fluid viscosities controls the stability of the invading fluid front [5–7]; and how the magnitude of the capillary number delineates distinct flow regimes [8, 9]. Each of the aforementioned controls is highly dependent on the system of interest, leading to significant non-linearity that complicates efforts to develop general relative permeability and capillary pressure models [10–13].

Flow of a *single fluid phase* through *deformable* porous media also has been studied in depth. Numerical modeling studies are largely based on the work of Biot and Terzaghi [14, 15] and have been used to reproduce the behavior of arteries, boreholes, swelling clays, and gels [16–19]. Other fundamental studies have examined the dynamics that arise from fluid-solid couplings beyond the ideal poroelastic regime, including fracturing, granular fingering, and frictional fingering [20–22]. They have

shown that the main parameters controlling the deformation of a porous solid by single phase flow are the material softness and the magnitude of the fluid-solid momentum transfer [21].

The study of *multiphase* flow in a *deformable* porous medium is inherently more complex than the problems outlined above, as it requires simultaneous consideration of capillarity, wetting dynamics, fluid rheology, and solid deformation. The few existing detailed examinations of this phenomenon have focused exclusively on the grain scale. In particular, Holtzman & Juanes [23, 24] used experiments and grain scale simulations to demonstrate that the transitions between capillary fingering, viscous fingering, and fracturing during multiphase flow in granular media reflect two non-dimensional numbers: a fracturing number (ratio of fluid driving force to solid cohesive force) and a modified capillary number. Other grain scale approaches have shown that fracturing is highly dependent on the invading fluid's capillary entry pressure [25, 26].

To the best of our knowledge, no experimental or numerical investigation has explored the effects of flow rate, wettability, and deformability during multiphase flow in deformable porous media within a *continuum scale* framework or identified the controlling parameters that relate *all three* properties within a comprehensive phase diagram. Here, we use simulations carried out with our novel multiphase Darcy-Brinkman-Biot (DBB) framework [27] to fill this knowledge gap and identify non-dimensional parameters that govern multiphase fluid invasion and fracturing in deformable porous media.

II. MODELING FRAMEWORK

Our investigation is carried out through the use of the Multiphase Darcy-Brinkman-Biot (DBB) modeling framework, a new and flexible model used to simulate two-phase flow through and around deformable porous

* <https://github.com/Franjcf>

† <http://bourg.princeton.edu>

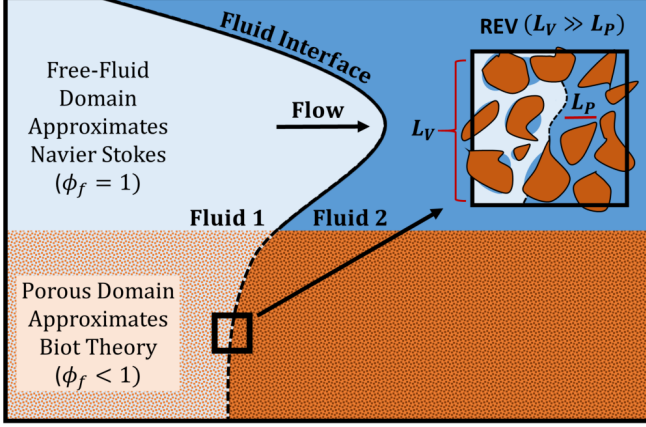


FIG. 1. Conceptual representation of the Multiphase DBB modelling framework. The porous domain is shown in the lower half (orange), the free-fluid domain is shown in the upper half (blue), the two immiscible fluids (left and right) are shown in different shades of blue and are separated by an interface (black), and ϕ_f is the porosity. REV is the “Representative Elementary Volume” over which all conservation equations are averaged.

media [27]. It consists of five volume averaged fluid and solid conservation equations that are coupled by spatially-dependent momentum exchange and capillary force terms. The model is comprised of a fluid mass conservation equation,

$$\frac{\partial \phi_f}{\partial t} + \nabla \cdot \mathbf{U}_f = 0 \quad (1)$$

a fluid saturation conservation equation,

$$\frac{\partial \phi_f \alpha_w}{\partial t} + \nabla \cdot (\alpha_w \mathbf{U}_f) + \nabla \cdot (\phi_f \alpha_w \alpha_n \mathbf{U}_r) = 0 \quad (2)$$

a fluid momentum conservation equation,

$$\begin{aligned} \frac{\partial \rho_f \mathbf{U}_f}{\partial t} + \nabla \cdot \left(\frac{\rho_f}{\phi_f} \mathbf{U}_f \mathbf{U}_f \right) &= -\phi_f \nabla p + \phi_f \rho_f \mathbf{g} + \\ \nabla \cdot \mathbf{S} - \phi_f \mu k^{-1} (\mathbf{U}_f - \mathbf{U}_s) + \phi_f \mathbf{F}_c - \phi_f p_c \nabla \alpha_w \end{aligned} \quad (3)$$

a solid mass conservation equation,

$$\frac{\partial \phi_s}{\partial t} + \nabla \cdot (\phi_s \mathbf{U}_s) = 0 \quad (4)$$

and a solid momentum conservation equation,

$$\begin{aligned} -\nabla \cdot \boldsymbol{\sigma} &= -\phi_s \nabla p + \phi_s \rho_s \mathbf{g} + \\ \phi_f \mu k^{-1} (\mathbf{U}_f - \mathbf{U}_s) - \phi_f \mathbf{F}_c - \phi_s p_c \nabla \alpha_w \end{aligned} \quad (5)$$

In the previous equations, ϕ_f is the fluid volume fraction, ϕ_s is the solid volume fraction, α_w is the wetting fluid saturation, α_n is the non-wetting fluid saturation, \mathbf{U}_f is the single-field fluid velocity, \mathbf{U}_s is the solid velocity, \mathbf{U}_r is the relative velocity of the two immiscible fluids, p is the single-field fluid pressure, \mathbf{S} is the volume

averaged fluid viscous stress tensor, $\boldsymbol{\sigma}$ is the volume averaged solid stress tensor, μk^{-1} is the drag coefficient (a function of permeability k and single-field fluid viscosity μ), ρ_s is the solid density, \mathbf{g} is gravity, p_c is the capillary pressure, and \mathbf{F}_c represents additional capillary terms. Lastly, $\rho_f = \alpha_w \rho_w + \alpha_n \rho_n$ and $\mu = \alpha_w \mu_w + \mu_n \rho_n$ are the single-field fluid density and viscosity. The closed form representations for \mathbf{U}_r , μk^{-1} , p_c , and \mathbf{F}_c can be found in the Supplemental Materials along with an in-depth description of the model.

As indicated in Fig. 1, the system of equations presented above asymptotically approaches the Navier-Stokes multiphase volume-of-fluid [28] equations in solid free regions (where $\phi_f = 1$, k is very large, and viscous drag is negligible) and multiphase Biot Theory in porous regions (where $\phi_f < 1$, k is small, $\text{Re} < 1$, and drag dominates). This last point can be demonstrated by adding Eqs. 3 and 5 together within a porous domain, which results in the main governing equation used in Biot Theory [27, 29, 30]:

$$\nabla \cdot \boldsymbol{\sigma} = \nabla p - (\phi_s \rho_s + \phi_f \rho_f) \mathbf{g} + p_c \nabla \alpha_w \quad (6)$$

A thorough discussion, derivation, and validation of this model can be found in Carrillo & Bourg 2020 [27] and related publications [18, 31]. We note that the following model considerations are required: (a) there needs to be a clear length-scale separation between the averaging volume, the sub-REV heterogeneities, and the overall system [32], and (b) closure of the system of equations necessitates the use parametric models that describe the average behaviour of the capillary pressure, permeability, and solid rheology within porous domains. As such, the inherent assumptions of these models should be adhered to. The complete numerical implementation of the solver, its validations, and the cases shown within this study can be found within the open-source simulation package “[hybridBiotInterFoam](#)” [33].

III. NUMERICAL SIMULATIONS

A. Crossover from Imbibition to Fracturing in a Hele-Shaw Cell

As a starting point, we applied the Multiphase DBB framework to model the crossover between fluid imbibition and fracturing in porous media. Here, the aim is to replicate experiments by Huang et. al. [34] involving the injection of aqueous glycerin into dry sand at incremental flowrates within a 30 by 30 by 2.5 cm Hele-Shaw cell. As shown in Fig. 2, these experiments are inherently multiphysics as fluid flow is governed by Stokes flow in the fracture (aperture \sim cm) and by multiphase Biot Theory in the porous sand (pore width \sim 100 μ m).

Numerical parameters were set to the known properties of aqueous glycerin, air, and sand ($\rho_{gly} = 1250 \text{ kg/m}^3$, $\mu_{gly} = 5 \text{ to } 176 \text{ cP}$, $\rho_{air} = 1 \text{ kg/m}^3$, $\mu_{air} = 0.017 \text{ cP}$, $\rho_s = 2650 \text{ kg/m}^3$), the air-glycerin surface tension $\gamma =$

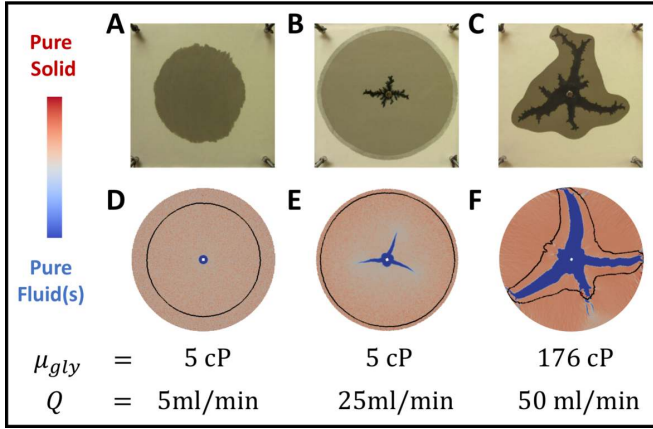


FIG. 2. Continuous transition from fluid imbibition to fracturing in a Hele-Shaw cell. Experimental images (A, B, C) were taken from Huang et. al. [34] and numerically replicated in this study using equivalent conditions (D, E, F). Black lines represent the advancing saturation front.

0.063 kg/s², and the sand grain radius $r_s = 100 \mu\text{m}$. To mimic the existence of sub-REV scale heterogeneity, the solid fraction was initialized as a normally-distributed field $\phi_s = 0.64 \pm 0.05$. To account for the non-reversible and compressive nature of the experiments, the deformable solid was modeled as a Hershel-Bulkley-Quemada plastic with yield stress $\tau_{yield} = 16.02 \text{ m}^2/\text{s}^2$ [27, 35, 36]. Permeability was modeled as a function of porosity through the Kozeny-Carman relation: $k = k_0 \phi_f^3 \phi_s^{-2}$ with $k_0 = 6.7 \times 10^{-12} \text{ m}^2$. Relative permeabilities were calculated through the Van Genutchen model [13] and capillary effects were assumed negligible.

The resulting simulations were implemented in OpenFOAM® within a 500 by 500 grid with constant flow boundary conditions at the inlet, zero-gradient flow conditions at the outlet, and no-slip boundary conditions for solid displacement at all boundaries. To allow for a proper comparison between 2-D simulations and 3-D experiments in a Hele-Shaw cell of thickness a , an additional drag term ($12\mu a^{-2} \mathbf{U}_f$) was included in the fluid momentum equation [37].

The similarities between our model and the experiments are evident: as the viscous forces imposed on the solid increase, so does the system's propensity to exhibit fracturing as the primary flow mechanism. Minor microstructural differences between our simulations and the experiments reflect the manner in which the continuum-scale solid rheology model approximates the solid's granular nature. It is clear, however, that both systems are controlled by the balance between viscous forces and solid rheology at the scale of interest [27].

B. Creation of Fracturing Phase Diagrams

We now use the simulation methodology presented above to identify the general non-dimensional parameters

that control the observed transitional behavior between invasion and fracturing. To do so, we systematically varied the solid's porosity ($\phi_f = 0.4$ to 0.8), plastic yield stress ($\tau_{yield} = 1.5$ to $24 \text{ m}^2/\text{s}^2$), capillary entry pressure ($p_{c,0} = 100$ to $50,000 \text{ Pa}$), and permeability ($k = 1 \times 10^{-13}$ and $5 \times 10^{-9} \text{ m}^2$) and the invading fluid's viscosity ($\mu_n = 0.5$ to 50 cP) and injection rate ($\mathbf{U}_f = 1 \times 10^{-4}$ to $8 \times 10^{-2} \text{ m/s}$). The only notable differences from the previous experiments are that we now include capillary effects and model drainage as opposed to imbibition (i.e., the injected glycerin is now non-wetting to the porous medium). A representative sample of the more than 400 resulting simulations is presented in the phase diagrams shown in Fig. 3.

Overall, the results make intuitive sense. Figure 3A shows that, *ceteris-paribus*, less permeable solids are more prone to fracturing. This is due to the fact that, given a constant flow rate, lower permeability solids experience greater drag forces. Our results also show that solids with lower plastic yield stresses fracture more readily, as their solid structure cannot withstand the effects of relatively large viscous or capillary forces. The y-axis behavior of Fig. 3B further shows that systems with higher entry pressures are more likely to fracture, i.e., the capillary stresses can overwhelm the solid's yield stress, in agreement with grain scale simulations [25]. Finally, Fig. 3B also shows that higher injection rates lead to more fracturing, as these increase the viscous drag effects on the solid structure.

IV. FORMULATION OF NON-DIMENSIONAL CONTROLLING PARAMETERS

The deformation regimes observed in the previous experiments can be delineated by defining two simple non-dimensional parameters that quantify the balance between viscous pressure drop, solid softness, and capillary entry pressure.

$$N_{vis} = \frac{\Delta p}{\tau_{yield} \rho_s} = \frac{\mu U L}{k \tau_{yield} \rho_s} \quad (\text{Cartesian}) \quad (7)$$

$$N_{vis} = \frac{\Delta p}{\tau_{yield} \rho_s} = \frac{\mu U r_{in}}{k \tau_{yield} \rho_s} \ln \left(\frac{r_{out}}{r_{in}} \right) \quad (\text{Radial}) \quad (8)$$

$$N_{cap} = \frac{p_{c,0}}{\tau_{yield} \rho_s} = \frac{2\gamma}{r_{pore} \tau_{yield} \rho_s} \quad (9)$$

Here, the viscous fracturing number (N_{vis}) represents the ratio between the viscous pressure drop and the solid's structural forces. It embodies the question: “Does fluid flow generate sufficient friction to induce fracturing?” As shown in Fig. 4, the answer is “No” if $N_{vis} < 1$ and “Yes” if $N_{vis} > 1$. This number is the continuum scale analog of the “fracturing number” presented by

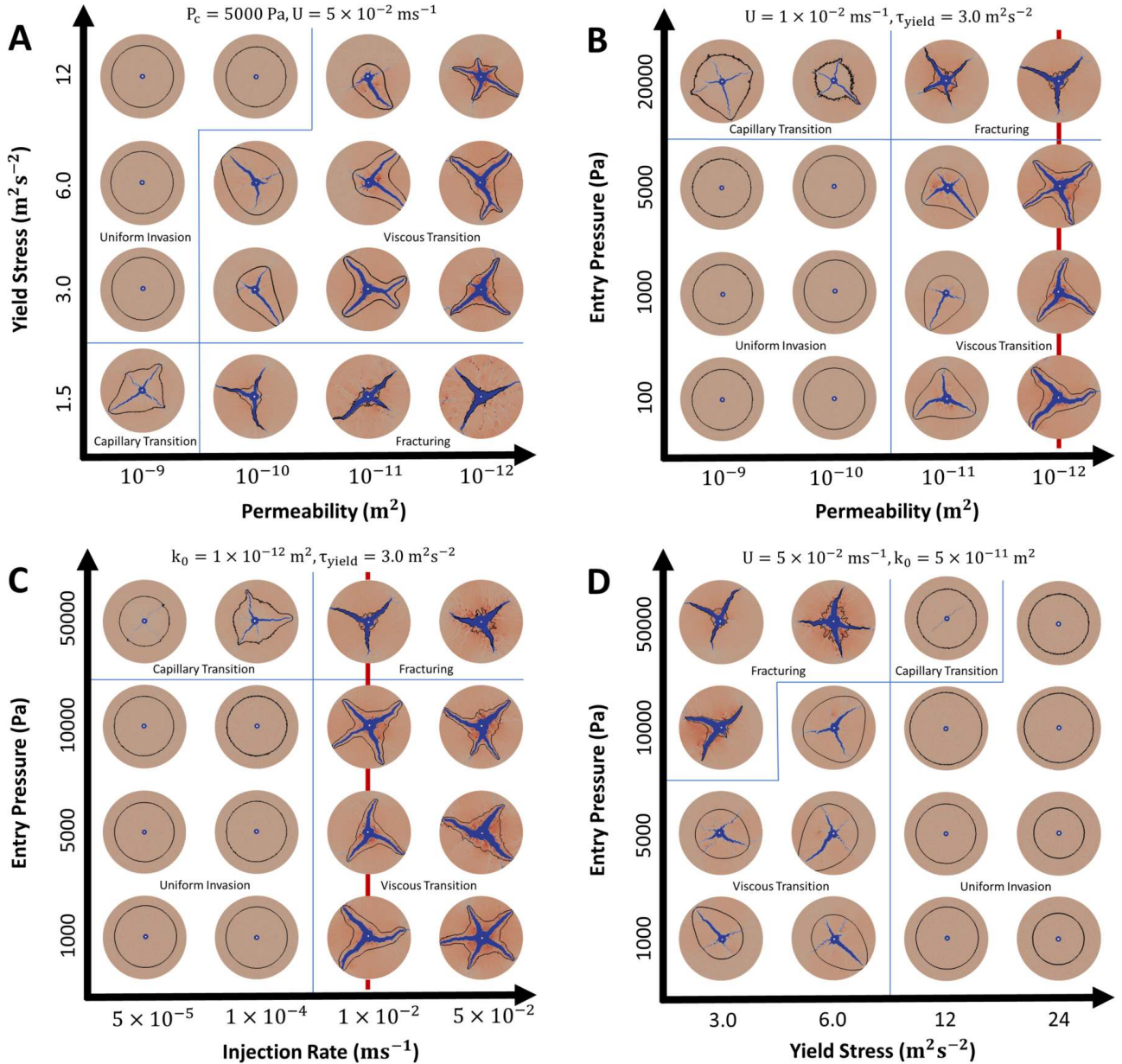


FIG. 3. Phase diagrams describing the effects of varying permeability, plastic yield stress, fluid injection rate, and capillary entry pressure on the transition from fluid drainage to fracturing. All cases are at $\phi_s = 0.60 \pm 0.05$ and $\mu_n = 5$ cP. The remaining parameters are case-specific and can be found in each figure's upper legend. The areas separated by thin blue lines highlight four deformation regimes referred to here as the uniform invasion, fracturing, viscous transition, and capillary transition regimes. The color scheme is the same as in Fig. 2.

Holtzman et. al. [24] for granular solids. It also explains the experimental finding by Zhou et. al. [38] that fracture initiation is only a function of pressure, irrespective of the injection fluid viscosity. Furthermore, it elucidates why increasing the injection rate and decreasing the permeability have similar effects in Fig. 3.

Complementarily, the capillary fracturing number (N_{cap}) represents the ratio between the capillary entry pressure and the solid's structural forces; it embodies the question: “Does multiphase flow generate sufficient cap-

illary stresses to fracture the solid?”. Figure 4 shows that when $N_{cap} < 1$ drainage is the preferential flow mechanism and when $N_{cap} > 1$ fracturing becomes the dominant phenomenon.

This analysis yields the rudimentary conclusion that uniform drainage should occur if either of the fracturing numbers is greater than unity, as confirmed by our simulations. However, our simulations further demonstrate the existence of three distinct fracturing regimes (Figs. 3-4). In the first regime, referred to here as the *fractur-*

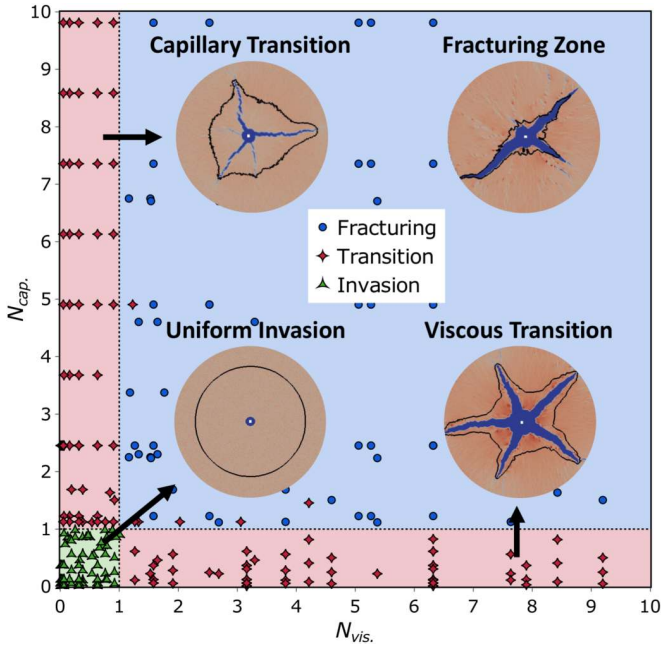


FIG. 4. Fluid invasion and fracturing in plastic porous media as a function of the viscous fracturing number N_{vis} and the capillary fracturing number N_{cap} . Green triangles denote uniform invasion, red diamonds denote the transitional field spaces, and blue circles denote pure fracturing.

ing zone, both fracturing numbers are greater than unity. This leads to fracturing of the porous solid with minimal capillary invasion. In the second regime, referred to here as the *viscous transition* ($N_{vis} > 1$ and $N_{cap} < 1$), only the viscous stresses are sufficiently large to fracture the solid. This leads to the formation of relatively wide fractures enveloped and preceded by a non-uniform invasion front. Finally, in the third regime, referred to here as the *capillary transition* ($N_{vis} < 1$ and $N_{cap} > 1$), only the capillary stresses are sufficiently large to fracture the solid. Given a constant injection rate, this leads to the formation of fractures preceded by an invasion front, as in the viscous transition regime, but with subtle differences. Notably, the saturation front is more uniform (because of the lower viscous stresses) and the solid exhibits less compaction and hence narrower fractures (capillary stresses are localized at the invasion front, whereas the viscous stresses are more broadly and increasingly distributed throughout the porous medium). Finally, we note that the crossover between each of the four regimes is continuous, meaning that systems with $N_{vis} \sim 1$ or $N_{cap} \sim 1$ can share elements of neighboring regimes.

V. INFLUENCE OF CAPILLARY HETEROGENEITY

Finally, we note that the simulations presented above were carried out using the simplifying assumption that the capillary pressure-saturation relationship is uniform

within the porous solid. To evaluate the impact of this simplification on the results shown in Figs. 3-4, we carried out additional simulations for all four regimes with a non-uniform capillary entry pressure distribution based on a simplified form of the well-known Leverett J-function where $p_{c,0} = p_{c,0}^*(\phi_s/\phi_s^{avg})^n$, $p_{c,0}^*$ is the capillary pressure at $\phi_s = \phi_s^{avg}$, and $n > 0$ is a sensitivity parameter [39, 40]. The results show that increasing the value of n stimulates the creation of finger-like instabilities at the fluid invasion front and leads to increased nucleation of small fractures at said position. Simulation predictions are shown in Fig. 5 in the case of the capillary transition regime with different n values. Despite the additional complexity of the resulting fluid invasion and fracturing patterns, our results with $n > 0$ are consistent with the overall phase diagram presented in Fig. 4. The results at $n = 0$ are therefore highlighted in this text due to the significantly greater simplicity of their fluid and solid distribution patterns.

VI. CONCLUSIONS

In this letter, we used the Multiphase DBB modeling framework to create a comprehensive phase diagram that identifies two non-dimensional parameters that categorize the crossover between fluid drainage and fracturing as a function of wettability, solid deformability, and hydrodynamics. In short, fracturing can occur whenever there is a high enough viscous and/or capillary pressure drop to overcome the solid structural forces. Furthermore, we showed that when it comes to systems with multiple fluids, it is also necessary to consider the effects of surface tension, wettability, and pore size into this analysis, as these parameters also control the fluids' propensity to fracture or invade the permeable solid. Lastly, we identified the theoretical existence of two characteristic transition zones between fluid invasion and fracturing that stem from the interplay of said fracturing numbers.

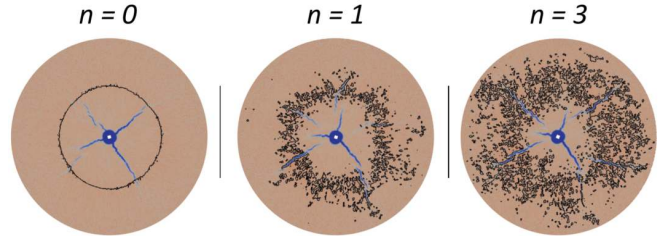


FIG. 5. The influence of capillary pressure heterogeneity on the capillary transition regime. Here, n represents the sensitive parameter in the Leverett J-function analogue. The color scheme is the same as in Fig. 2.

ACKNOWLEDGMENTS

This work was supported by the National Science Foundation, Division of Earth Sciences, Early Career

program through Award EAR-1752982, and by the Mary and Randall Hack '69 Research Fund provided by the High Meadows Environmental Institute at Princeton University.

[1] C. Bächer and S. Gekle, Computational modeling of active deformable membranes embedded in three-dimensional flows, *Physical Review E* **99**, 062418 (2019).

[2] L. Räss, N. S. Simon, and Y. Y. Podladchikov, Spontaneous formation of fluid escape pipes from subsurface reservoirs, *Scientific Reports* **8**, 1 (2018).

[3] G. D. Towner, The mechanics of cracking of drying clay, *Journal of Agricultural Engineering Research* **36**, 115 (1987).

[4] R. Lenormand, Pattern growth and fluid displacements through porous media, *Physica A: Statistical Mechanics and its Applications* **140**, 114 (1986).

[5] K. J. Måløy, J. Feder, and T. Jøssang, Viscous Fingering Fractals in Porous Media, *Physical Review Letters* **55**, 24 (1985).

[6] P. Saffman and G. Taylor, The penetration of a fluid into a porous medium or Hele-Shaw cell containing a more viscous liquid, *Dynamics of Curved Fronts* **245**, 155 (1988).

[7] J. P. Stokes, D. A. Weitz, J. P. Gollub, A. Dougherty, M. O. Robbins, P. M. Chaikin, and H. M. Lindsay, Interfacial stability of immiscible displacement in a porous medium, *Physical Review Letters* **57**, 1718 (1986).

[8] M. Ferer, C. Ji, G. S. Bromhal, J. Cook, G. Ahmadi, and D. H. Smith, Crossover from capillary fingering to viscous fingering for immiscible unstable flow: Experiment and modeling, *Physical Review E - Statistical Physics, Plasmas, Fluids, and Related Interdisciplinary Topics* **70**, 7 (2004).

[9] Y. C. Yortsos, B. Xu, and D. Salin, Phase Diagram of Fully Developed Drainage in Porous Media, *Physical Review Letters* **79** (1997).

[10] D. Picchi and I. Battiato, The Impact of Pore-Scale Flow Regimes on Upscaling of Immiscible Two-Phase Flow in Porous Media, *Water Resources Research* **54**, 6683 (2018).

[11] D. Picchi and I. Battiato, Relative Permeability Scaling From Pore-Scale Flow Regimes, *Water Resources Research* **55**, 3215 (2019).

[12] R. Brooks and A. Corey, Hydraulic Properties of Porous Media, *Hydrology Papers, Colorado State University* **3**, 37 pp (1964).

[13] M. T. van Genuchten, A Closed-form Equation for Predicting the Hydraulic Conductivity of Unsaturated Soils, *Soil Science Society of America Journal* **44**, 892 (1980).

[14] M. A. Biot, General Theory of Three-Dimensional Consolidation, *Journal of Applied Physics* **12**, 155 (1941).

[15] K. Terzaghi, *Theoretical Soil Mechanics* (John Wiley & Sons, Inc., Hoboken, NJ, USA, 1943).

[16] L. C. Auton and C. W. MacMinn, From arteries to boreholes: steady-state response of a poroelastic cylinder to fluid injection, *Proceedings of the Royal Society A: Mathematical, Physical and Engineering Science* **473**, 20160753 (2017), arXiv:1609.09457.

[17] T. Bertrand, J. Peixinho, S. Mukhopadhyay, and C. W. MacMinn, Dynamics of Swelling and Drying in a Spherical Gel, *Physical Review Applied* **6**, 064010 (2016), arXiv:1605.00599.

[18] F. J. Carrillo and I. C. Bourg, A Darcy-Brinkman-Biot Approach to Modeling the Hydrology and Mechanics of Porous Media Containing Macropores and Deformable Microporous Regions, *Water Resources Research* **55**, 8096 (2019).

[19] C. W. MacMinn, E. R. Dufresne, and J. S. Wetzlaufer, Fluid-driven deformation of a soft granular material, *Physical Review X* **5**, 011020 (2015), arXiv:1405.7311.

[20] J. M. Campbell, D. Ozturk, and B. Sandnes, Gas-Driven Fracturing of Saturated Granular Media, *Physical Review Applied* **8**, 10.1103/PhysRevApplied.8.064029 (2017).

[21] B. Sandnes, E. G. Flekkøy, H. A. Knudsen, K. J. Måløy, and H. See, Patterns and flow in frictional fluid dynamics, *Nature Communications* **2**, 10.1038/ncomms1289 (2011).

[22] F. Zhang, Pattern formation in fluid injection into dense granular media, *Géotechnique* **29**, 47 (2012).

[23] R. Holtzman and R. Juanes, Crossover from fingering to fracturing in deformable disordered media, *Physical Review E - Statistical, Nonlinear, and Soft Matter Physics* **82**, 10.1103/PhysRevE.82.046305 (2010).

[24] R. Holtzman, M. L. Szulczewski, and R. Juanes, Capillary fracturing in granular media, *Physical Review Letters* **108**, 10.1103/PhysRevLett.108.264504 (2012).

[25] A. K. Jain and R. Juanes, Preferential mode of gas invasion in sediments: Grain-scale mechanistic model of coupled multiphase fluid flow and sediment mechanics, *Journal of Geophysical Research: Solid Earth* **114**, 1 (2009).

[26] Y. Meng, B. K. Primkulov, Z. Yang, C. Y. Kwok, and R. Juanes, Jamming transition and emergence of fracturing in wet granular media, *Physical Review Research* **2**, 022012 (2020).

[27] F. J. Carrillo and I. C. Bourg, Modeling multiphase flow within and around deformable porous materials: A darcy-brinkman-biot approach, *Earth and Space Science Open Archive* , 33 (2020).

[28] C. W. Hirt and B. D. Nichols, Volume of Fluid (VOF) Method for the Dynamics of Free Boundaries, *Journal of Computational Physics* **39**, 201 (1981).

[29] B. Jha and R. Juanes, Coupled multiphase flow and poromechanics: A computational model of pore pressure effects on fault slip and earthquake triggering, *Water Resources Research* **50**, 3776 (2014), arXiv:2014WR016527 [10.1002].

[30] J. Kim, H. A. Tchelepi, and R. Juanes, Rigorous coupling of geomechanics and multiphase flow with strong capillarity, *SPE Journal* **18**, 1123 (2013).

[31] F. J. Carrillo, I. C. Bourg, and C. Soulaine, Multiphase Flow Modelling in Multiscale Porous Media: An Open-Sourced Micro-Continuum Approach, *Journal of Computational Physics: X* , 100073 (2020), arXiv:2003.08374.

[32] S. Whitaker, Flow in porous media I: A theoretical derivation of Darcy's law, *Transport in Porous Media* **1**,

3 (1986).

[33] F. J. Carrillo and I. C. Bourg, *hybridBiotInterFoam* (2020).

[34] H. Huang, F. Zhang, P. Callahan, and J. Ayoub, Fluid injection experiments in 2D porous media, in *SPE Journal*, Vol. 17 (2012) pp. 903–911.

[35] A.-S. Ahmed, Z. Karim, W. Gay, M. Fanhong, and S. Manoj, Fracture Propagation and Formation Disturbance during Injection and Frac-Pack Operations in Soft Compacting Rocks, in *Proceedings - SPE Annual Technical Conference and Exhibition* (Society of Petroleum Engineers, 2007) pp. 3453–3464.

[36] D. B. van Dam, P. Papanastasiou, and C. J. de Pater, Impact of rock plasticity on hydraulic fracture propagation and closure, *SPE Production and Facilities* **17**, 149 (2002).

[37] A. Ferrari, J. Jimenez-Martinez, T. Le Borgne, Y. Méheust, and I. Lunati, Challenges in modeling unstable two-phase flow experiments in porous micromodels, *Water Resources Research* **51**, 1381 (2015).

[38] J. Zhou, Y. Dong, C. J. De Pater, and P. L. Zitha, Experimental study of the impact of shear dilation and fracture behavior during polymer injection for heavy oil recovery in unconsolidated reservoirs, in *Society of Petroleum Engineers - Canadian Unconventional Resources and International Petroleum Conference 2010*, Vol. 3 (2010) pp. 1886–1897.

[39] M. Leverett, Capillary Behavior in Porous Solids, *Transactions of the AIME* **142**, 152 (1941).

[40] B. Li and S. M. Benson, Influence of small-scale heterogeneity on upward CO₂plume migration in storage aquifers, *Advances in Water Resources* **83**, 389 (2015).

Supplementary Materials for: “Capillary and Viscous Fracturing During Drainage in Porous Media”

Francisco J. Carrillo^a, Ian C. Bourg^{b,c}

^aDepartment of Chemical and Biological Engineering, Princeton University, Princeton, NJ, USA

^bDepartment of Civil and Environmental Engineering, Princeton University, Princeton, NJ, USA

^cPrinceton Environmental Institute, Princeton University, Princeton, NJ, USA

Abstract

This Supplementary Material consists of the following:

1. A [Section](#) describing the fully-coupled model for two-phase flow and solid mechanics.
2. A [Section](#) that outlines the solid’s plastic rheology model.
3. A [Table](#) defining all the symbols used throughout the text.

1. Complete Description of Modelling Framework

The complete set of equations in the multiphase Darcy-Brinkman-Biot framework now follows. The combination of these solid and fluid conservation equations leads to a model that tends towards multiphase Navier-Stokes in solid-free regions and towards Biot Theory in porous regions, as described in Figure 1 in the main text.

$$\frac{\partial \phi_f}{\partial t} + \nabla \cdot \mathbf{U}_f = 0 \quad (1)$$

$$\frac{\partial \phi_f \alpha_w}{\partial t} + \nabla \cdot (\alpha_w \mathbf{U}_f) + \nabla \cdot (\phi_f \alpha_w \alpha_n \mathbf{U}_r) = 0 \quad (2)$$

$$\begin{aligned} \frac{\partial \rho_f \mathbf{U}_f}{\partial t} + \nabla \cdot \left(\frac{\rho_f}{\phi_f} \mathbf{U}_f \mathbf{U}_f \right) = & -\phi_f \nabla p + \phi_f \rho_f \mathbf{g} + \nabla \cdot \mathbf{S} \\ & - \phi_f \mu k^{-1} (\mathbf{U}_f - \mathbf{U}_s) + \phi_f \mathbf{F}_{c,1} + \phi_f \mathbf{F}_{c,2} \end{aligned} \quad (3)$$

$$\frac{\partial \phi_s}{\partial t} + \nabla \cdot (\phi_s \mathbf{U}_s) = 0 \quad (4)$$

$$-\nabla \cdot \bar{\boldsymbol{\sigma}} = -\phi_s \nabla p + \phi_s \rho_s \mathbf{g} + \phi_f \mu k^{-1} (\mathbf{U}_f - \mathbf{U}_s) - \phi_f \mathbf{F}_{c,1} + \phi_s \mathbf{F}_{c,2} \quad (5)$$

We now state the closed-form expressions of the multiscale parameters μk^{-1} , $\mathbf{F}_{c,i}$, and \mathbf{U}_r , which are defined differently in each region. A full derivation and discussion of these parameters can be found in [Carrillo et al. \(2020\)](#) and [Carrillo and Bourg \(2020b\)](#).

$$\mu k^{-1} = \begin{cases} 0 & \text{in solid-free regions} \\ k_0^{-1} \left(\frac{k_{r,w}}{\mu_w} + \frac{k_{r,n}}{\mu_n} \right)^{-1} & \text{in porous regions} \end{cases} \quad (6)$$

$$\mathbf{F}_{c,1} = \begin{cases} -\frac{\gamma}{\phi_f} \nabla \cdot (\mathbf{n}_{w,n}) \nabla \alpha_w & \text{in solid-free regions} \\ -p_c \nabla \alpha_w & \text{in porous regions} \end{cases} \quad (7)$$

$$\mathbf{F}_{c,2} = \begin{cases} 0 & \text{in solid-free regions} \\ M^{-1} (M_w \alpha_n - M_n \alpha_w) (\nabla p_c + (\rho_w - \rho_n) \mathbf{g}) & \text{in porous regions} \end{cases} \quad (8)$$

$$\mathbf{n}_{w,n} = \begin{cases} \frac{\nabla \alpha_w}{|\nabla \alpha_w|} & \text{in solid-free regions} \\ \cos(\theta) \mathbf{n}_{wall} + \sin(\theta) \mathbf{t}_{wall} & \text{at the interface between solid-free porous regions} \end{cases} \quad (9)$$

$$\mathbf{U}_r = \begin{cases} C_\alpha \max(|\mathbf{U}_f|) \frac{\nabla \alpha_w}{|\nabla \alpha_w|} & \text{in solid-free regions} \\ \phi^{-1} \left[\begin{array}{l} - (M_w \alpha_w^{-1} - M_n \alpha_n^{-1}) \nabla p + (\rho_w M_w \alpha_w^{-1} - \rho_n M_n \alpha_n^{-1}) \mathbf{g} \\ (M_w \alpha_n \alpha_w^{-1} + M_n \alpha_w \alpha_n^{-1}) \nabla p_c - (M_w \alpha_w^{-1} - M_n \alpha_n^{-1}) p_c \nabla \alpha_w \end{array} \right] & \text{in porous regions} \end{cases} \quad (10)$$

where C_α is an interface compression parameter (traditionally set to values between 1 and 4 in the Volume-of-Fluid method), k_0 is the absolute permeability, $k_{r,i}$ and $M_i = k_0 k_{i,r} / \mu_i$ are the relative permeability and mobility of each fluid, and $M = M_w + M_n$. Lastly, θ is the imposed contact angle at the porous wall, and \mathbf{n}_{wall} and \mathbf{t}_{wall} are the normal and tangential directions relative to said wall, respectively.

Closure of this system of equations requires appropriate constitutive models describing the averaged behavior of the different phases within the porous regions. In the present paper we use the following well established constitutive models: absolute permeability is modeled as isotropic and porosity-dependent through the Kozeny-Carman relation ($k_0 = k_0^0 \frac{\phi_f^3}{(1-\phi_f)^2}$); relative permeabilities and average capillary pressures within the porous domains are represented using the well-known Van Genuchten (van Genuchten, 1980) model; plasticity is described through the Herschel-Bulkley model, were the solid viscously deforms only after local stresses become higher than the material yield stress; finally the solid's yield stress and plastic viscosity are modeled as solid fraction-dependent based on the Quemada fractal model (Quemada, 1977; Spearman, 2017). For the reader's convenience, a full implementation of this framework and its related models are included in the accompanying code (Carrillo and Bourg, 2020a).

2. Solid Rheology Models

2.1. Hershel-Bulkley Plasticity

A Bingham plastic is a material that deforms only once it is under a sufficiently high stress. After this yield stress is reached, it will deform viscously and irreversibly. The Herschel-Bulkley rheological model combines the properties of a Bingham plastic with a power-law viscosity model, such that said plastic can be shear thinning or shear thickening during deformation. In OpenFOAM® this model is implemented as follows:

$$\boldsymbol{\sigma} = \mu_s^{eff} \left(\nabla \mathbf{U}_s + (\nabla \mathbf{U}_s)^T - \frac{2}{3} \nabla \cdot (\mathbf{U}_s \mathbf{I}) \right)$$

where μ_s^{eff} is the effective solid plastic viscosity, which is then modeled through a power law expression:

$$\mu_s^{eff} = \min \left(\mu_s^0, \frac{\tau}{\eta} + \mu_s \eta^{n-1} \right)$$

where μ_s^0 is the limiting viscosity (set to a large value), τ is the yield stress, μ_s is the viscosity of the solid once the yield stress is overcome, n is the flow index ($n = 1$ for constant viscosity), and η is the shear rate.

2.2. Quemada Rheology Model

The Quemada rheology model [Quemada \(1977\)](#); [Spearman \(2017\)](#) is a simple model that accounts for the fact that the average yield stress and effective viscosity of a plastic are functions of the solid fraction. These two quantities are large at high solid fractions and small at low solid fractions, as described by the following relations

$$\tau = \tau_0 \left(\frac{(\phi_s / \phi_s^{max})}{(1 - \phi_s / \phi_s^{max})} \right)^D$$

$$\mu_s = \frac{\mu_0}{\left(1 - \frac{\phi_s}{\phi_s^{max}} \right)^2}$$

here, ϕ_s^{max} is the maximum solid fraction possible (perfect incompressible packing), τ_0 is the yield stress at $\phi_s = \phi_s^{max}/2$, μ_0 is the viscosity of the fluid where the solid would be suspended at low solid fractions (high fluid fractions), and D is a scaling parameter based on the solid's fractal dimension.

References

References

Carrillo, F. J., Bourg, I. C., sep 2020a. hybridBiotInterFoam.
URL <https://zenodo.org/record/4013969>

Carrillo, F. J., Bourg, I. C., 2020b. Modeling multiphase flow within and around deformable porous materials: A darcy-brinkman-biot approach. *Earth and Space Science Open Archive*, 33.
URL <https://www.essuar.org/doi/abs/10.1002/essoar.10504277.2>

Carrillo, F. J., Bourg, I. C., Soulaine, C., sep 2020. Multiphase Flow Modelling in Multiscale Porous Media: An Open-Sourced Micro-Continuum Approach. *Journal of Computational Physics*: X, 100073.

Quemada, D., jan 1977. Rheology of concentrated disperse systems and minimum energy dissipation principle - I. Viscosity-concentration relationship. *Rheologica Acta* 16 (1), 82–94.

Spearman, J., 2017. An examination of the rheology of flocculated clay suspensions. *Ocean Dynamics* 67 (3-4), 485–497.

van Genuchten, M. T., 1980. A Closed-form Equation for Predicting the Hydraulic Conductivity of Unsaturated Soils. *Soil Science Society of America Journal* 44 (5), 892–898.